Wavelength and energy dependence on ablation dynamics under femtosecond laser pulses observed by time-resolved pump–probe microscopy

I. M. Carrasco-García, J. M. Vadillo, J. J. Laserna
Universidad de Málaga, UMA LASERLAB, Jimenez Fraud 4, ES 29010, Spain

ABSTRACT

Pump–probe femtosecond microscopy has been applied to reveal the time evolution of the ablation processes at sub-picosecond resolution with combined pulses of different photon energies. Experimental results revealed that differences in the photon energies of ablation pulses influenced the temporal response of the material. Significant differences in the excitation and melting of the material within 10 ps of irradiation were observed. The analysis of dynamic Newton's rings observed with the pump–probe technique confirmed and explained the faster expansion of ablated matter when using shorter irradiation wavelengths. The results also implied that optical properties of the material play a significant role.

INTRODUCTION

Laser-based techniques allow the modification of materials in the melting, spallation, and ablation regimes, which includes the gentle removal of just a few atoms or molecules to a high material mass removal rates. Several different analysis techniques have been used in an effort to visualize and understand the phenomena involved in the interaction of a femtosecond laser pulse with solid matter from surface emission up to permanent damage. Depending on the intended application of laser ablation, different characteristics of the laser pulse will be of more interest. Various studies over the last decades have investigated the influence of the pulse width (1-5). Ablation with nanosecond lasers is dominated by laser–matter and laser–plasma processes, as the pulse duration is long enough that it persists as evaporation of material is taking place. These processes affect the total deposition of energy on the target, which influences the resulting crater and damage formation (6). The key difference with femtosecond pulses is that the laser–matter interaction is shorter in time than all the processes induced by this interaction which, among other advantages, results in material being removed only from a confined region corresponding to the irradiated area (5, 7-8).

The influence of the laser wavelength on the properties of the plasmas produced when using short pulses to irradiate the target (9-14), have been studied from the point of view of the acquisition of LIBS spectra. In the case of ultrashort pulses, different experimental techniques including filamentation LIBS (15-17), ICP (18), and micromachining and drilling (12) have been applied to investigate the role of this parameter. Different analysis techniques can help reveal the processes dominant during ablation; for example, by the application of fast image acquisition, as shadowgraphy, or the use of streak cameras (19-21). Although these visualize the processes that induce ablation, they do not show what is happening in the structure of the material. Pump–probe microscopy has proved to be a useful and robust tool to monitor phase-change processes (22-28). The use of femtosecond laser pulses for both ablating and probing the irradiated target offers a temporal resolution limited by the pulse width, providing deeper insight into the processes involved in ablation and plasma formation. Additionally, the absence of laser–plasma interaction when using femtosecond pulses, makes it possible to deposit more laser energy into the target compared to longer laser pulses (29,30). The process occurring on dielectrics are complex and demand high energy densities to occur (31-33) while on metals, due to the absence of a band gap in their electronic configuration, the main mechanism of energy absorption is by free carriers, so less energy is required from the laser pulse to induce the ablation (29, 34-36).

The present study applies time-resolved pump–probe microscopy to determine the effect of irradiation wavelength on the processes taking place prior to plasma formation during femtosecond laser ablation. Time-resolved pump–probe microscopy provides insight into the morphological dynamics of the material with high temporal resolution. Gold has been used as test sample due to its significant different reflectance behavior along the UV-VIS spectra and the easiness in the fabrication of smooth thin layers with minimum scattering effect due to sample roughness. Relevant differences, even at sub-picosecond times, are reported, highlighting the importance of the optical properties of the material.

EXPERIMENTAL SET-UP

The experimental set-up has been described in detail in previous references (27,28). Briefly, it consists of an regeneratively-amplified Ti:Sa laser providing p-polarized 35 fs FWHM pulses at 800 nm with a mean energy of 3.5 mJ. By means of a 80/20 beam splitter and two optical delay lines, two independent laser branches (pump and probe) arrive the sample at selectable times. The temporal precision that can be achieved with these two stages is 6.67 fs, so the temporal resolution of the experiment is ultimately limited by the length of the laser pulses. The energy of the pump beam and probe beams are controlled by optical attenuator, and pulses are focused onto the target by a plano-convex lens with a 150 mm focal length. In all the circumstances, the probe beam is adjusted below the ablation threshold. An electromechanical shutter ensures that only a single pump pulse irradiates the target for each event. A harmonic generator allows the transformation of an incomimg beam at 800 nm into two beams at 400 nm and 266 nm.

Light reflected by the target passes back through the microscope objective and is reflected by a dichroic mirror and finally focused onto a 10-bit CMOS camera synchronized (As the shutter) by the laser amplifier. Specific dichroic mirrors, bandpass filters and polarizing elements were added for the different combinations of 800, 400 and 266 nm wavelengths for the pump and probe beams as detailed in Figure 1.

The samples studied in the present work were 200 nm thick gold films deposited on glass substrates by DC sputtering. The roughness of the films was lower than 5 nm, as measured by atomic force microscopy. A fresh part of the sample surface was used for each laser event. Three images of the surface were acquired for every event: the first image recorded the sample surface prior to irradiation; the second image corresponds to the arrival of the probe beam with a predetermined delay relative to the pump beam, and captures the process as it takes place; the third image is taken several seconds after irradiation, and shows the permanent damage to the sample surface. Images corresponding to each laser shot were processed using a custom MATLAB script, which displays the first and second images and allowing the user to select the area of interest where ablation is observed. The script then outputs the normalized reflectivity.

RESULTS AND DISCUSSION

Three main stages can generally be distinguished during femtosecond laser ablation, although these may be initiated by different mechanisms depending on the nature of the target (29, 37-39). The first process is excitation, which is characterized by a bright area where the laser pulse impinges on the sample. In this stage, lattice electrons are excited by the laser's electric field and promoted from the valence band to the conduction band by multiphoton ionization or inverse Bremsstrahlung. This increases the free electron population and can be observed as an increase in the reflectivity of the target. Subsequently, after a few tens of picoseconds, target melting starts, accompanied by a dramatic decrease of the reflectivity which manifests itself as an expanding dark area. In contrast to excitation, this dark area grows radially outwards, as all electrons in the irradiated area are excited by this time. This melting results from relaxation processes such as electron–phonon collision, with different pathways active depending on the input energy and the characteristics of the lattice (29, 39-40). These collision processes result in a melting front propagating through the irradiated volume. Once the melting front reaches the bulk–molten material interface, expansion begins. In this stage, under certain conditions of the absence of roughness, ring patterns which evolve with time have been observed (26, 27, 41, 42). These arise due to differences between the refractive indices of the external layer, which remains in a solid–liquid state, and the vaporized material contained between this layer and the non-ablated material.

Schematic side and top-down views of these processes are shown in Figure 2.; the top-down views in the bottom row illustrate the changes in reflectivity produced by the interaction of the probe beam with the target. During excitation, the increased electron population at the surface causes an increase in the reflectivity, which remains until electron de-excitation occurs. On the other hand, material melting, caused by de-excitation of electrons by collision processes, is observed as a decrease in the reflectivity of the sample, starting in the center of the irradiated area and growing radially. Finally, once surface deformation starts, the outer surface of the target consists of a mixture of solid and liquid phases encapsulating the vaporized material and resultant voids, ultimately giving rise to the dynamic Newton's rings patterns.

Schematic side and top-down views of these processes are shown in Figure 2; the top-down views in the bottom row illustrate the changes in reflectivity produced by the interaction of the probe beam with the target. During excitation, the increased electron population at the surface causes an increase in the reflectivity, which remains until electron de-excitation occurs. On the other hand, material melting, caused by de-excitation of electrons by collision processes, is observed as a decrease in the reflectivity of the sample, starting in the center of the irradiated area and growing radially. Finally, once surface deformation starts, the outer surface of the target consists of a mixture of solid and liquid phases encapsulating the vaporized material and resultant voids, ultimately giving rise to the dynamic Newton's rings patterns.

Figure 3 shows different time-resolved micrographs to compare the evolution of the surface of irradiated material when using each of the three harmonics as pump irradiation. The pump energy was fixed at 20 µJ, and 400 nm light was used as the probe beam. Contrast and brightness have been enhanced identically in the three situations in order to make the differences more visible. As observed, pump-probe time-resolved micrography allows the visualization of the sequential excitation, melting and vaporization processes and the differences derived on the photon energy to excite the sample. Thus, a local increase of the reflectivity of the irradiated area is produced in the first picosecond after irradiation for all experiments. The comparison of the micrographs at 2 ps reveals clearly the larger reflectivity as the pump wavelength decreases.

Once the melting front reaches the interface with the bulk material, it is reflected and the target starts to deform, as depicted in Figure 2. Target deformation produces a multilayer system at the target surface, giving rise to Newton's rings. These start to develop earlier (~ 1 ns) for shorter wavelengths, while are barely seen at 800 nm. The transmission of more energy from electrons to phonons induces faster melting of the material, forcing the vaporized material encapsulated by the target surface to expands faster. The result is a more pronounced curvature of the surface dome yielding more numerous and more closely-spaced the Newton's rings. At 800 nm, no evidence of Newton's rings is observed in the interval studied.

A detailed intensity profile of the different micrographs covering the timescale from time zero to 2 ns is found in Figure 4. The plot shows the normalized intensity as well as the error bars for three replicated measurements processed with the MATLAB script detailed in the experimental section. In all the cases, an identical central region on each image was considered for computing.

For 266 excitation (solid triangles), it is quite evident the significant increase in reflectivity observed up to 2 ps after irradiation, in consonance with the large target excitation at such wavelength. After excitation, melting proceeds at fast rate due to the high electron density which increases the rate of electron–phonon collisions. Similar results are found at 400 nm (open squares), also exhibiting (although less pronounced) an increase of reflectivity due to electron excitation, with a maximum reflectivity around 1 ps earlier than for the measurements using the 266 nm wavelength. The maximum reflectivity was lower for 400 nm irradiation, explainable due to the lower photon energy. These measurements were repeated at half the energy at both wavelengths without any significant change in the behavior. In both cases, the error bars correspond to the averaging of three replicated measurements. For 800 nm irradiation, it is quite evident the plateau-like behavior of the surface reflectivity during the first 10 ps, confirming that irradiation at longer wavelengths requires a higher number of photons to induce sample excitation.

The role of the probe beam can´t be ruled out in our time-resolved microscope. To check its effect, an experiment was performed with permuted 400 and 800 nm beams as pump and probe beams. This combination was chosen due to the large differences in reflectivity of gold for such wavelength as can be seen in Figure 5, where the reflectivity of Ag and Al are included for comparison. As observed, Au reflectivity at 800 nm is close to 98% while at 400 nm is around 37%. Figure 6 shows the time evolution of the normalized reflectivity using permuted 800/400 and 400/800 pump–probe configurations at higher photon densities compared to the one used in Figure 4. As shown for the 800/400 pump/probe squeme (circles) an increase in the reflectivity is observed during excitation at times before 1 ps, followed by a decrease in reflectivity associated with melting of the target. At a difference of the results in Figure 4, the increased photon density has been high enough to induce the ablation in the target. Although not calculated for this work, it seems evident the existence of a wavelength-specific threshold energy value. The dependence of such value with sample type or sample conditions are out of the scope of this work, although a previous references (43) dealing with the calculation of plasma ignition threshold fluence values by means of optical emission spectroscopy for different metals revealed a dependence with the work function. The correlation between the plasma formation values and our time-resolved reflectivity measurements is yet to be calculated in future works. Concerning the 400/800 configuration (squared symbols in Figure 6), despite the higher photon density, a plateau is observed, while in Figure 4 (with a 400/400 configuration and 20 μJ of pulse energy) a clear increase in reflectivity with a maximum at 1 ps is observed. The difference in the results observed when using a 400 nm and 800 nm pump and probe respectively can be explained based on the natural reflectivity of the material. The probe pulses reflect the transient processes taking place in the irradiated material. Under 800 nm probe conditions, the native sample reflectivity will be that high that any reflectivity increase will be barely detectable.

Conclusions

The effect of photon energy during femtosecond laser irradiation was studied using time-resolved pump–probe microscopy. It was found that during the excitation stage, the pump wavelength induces differences in excitation time, but that this is also influenced by the optical properties of the material, as the penetration depth and native reflectivity of the sample also play a role. Melting and expansion of the irradiated material were also investigated by the analysis of Newton’s rings, but the most relevant parameters in these stages proved to be the photon energy and photon density. The role of the probe wavelength was also studied under different conditions. The higher reflectivity of gold at 800 nm means that an increase in reflectivity as the sample is excited by femtosecond pulses is not observed, even when increasing pump pulse energy, although the Newton’s rings grow faster. The latter demonstrates the faster expansion of the ablated material when the material is irradiated using shorter wavelengths.

Acknowledgments

This work was funded by the Spanish Ministry of Economy and Competitiveness (MINECO) through projects CTQ2011-24433, CTQ2014-56058P and CTQ2017-82137-P. One of the authors (ICG) acknowledges financial support for her doctoral work through the Programa de Formación de Personal Investigador

References

1 Chichkov, B.N., Momma, C., Nolte, S. et al. Appl. Phys. A (1996) 63: 109. Femtosecond, picosecond and nanosecond laser ablation of solids. https://doi.org/10.1007/BF01567637

2 Ashkenasi, D., Rosenfeld, A. et al. Appl Phys A (1997) 65: 367. Micromachining of quartz with ultrashort laser pulses. Varel, H., https://doi.org/10.1007/s003390050593

3 Ablation characteristics of Au, Ag, and Cu metals using a femtosecond Ti:sapphire laser. Furusawa, K., Takahashi, K., Kumagai, H. et al. Appl Phys A (1999) 69(Suppl 1): S359. https://doi.org/10.1007/s003390051417

4 Ablation threshold dependence on pulse duration for copper. Hashida, D., Semerok A. F., Gobert, O., Petite, G., Izawa, Y., Wagner, J. F. Appl. Sur. Sci (2002) 197, 862 **https://doi.org/10.1016/S0169-4332(02)00463-4**

5 Femtosecond time-resolved laser-induced breakdown spectroscopy for detection and identification of bacteria: A comparison to the nanosecond regime. Baudelet, M., Guyon, L., Yu, J., Wolf J. P., Amodeo, T., Fréjafon, E., Laloi P. Journal of Applied Physics 99, 084701 (2006); doi: 10.1063/1.2187107

6 R. E. Russo, X. Mao, J. J. Gonzalez, V. Zorba†, J. Yoo. Laser ablation in analytical chemistry. Anal. Chem. (2013), 85, 13, 6162-6177, https://dx.doi.org/10.1021/ac4005327

7 M. Guillermin, J. P. Colombier, S. Valette, E. Audouard, F. Garrelie, and R. Stoian. Optical emission and nanoparticle generation in Al plasmas using ultrashort laser pulses temporally optimized by real-time spectroscopic feedback. Phys. Rev. B (2010) 82, 035430

8 Forster, M., Égerházi, L., Haselberger, C. et al. Femtosecond laser interaction with pulsed-laser deposited carbon thin films of nanoscale thickness Appl. Phys. A (2011) 102: 27. https://doi.org/10.1007/s00339-010-6013-5

9 L.M.CabalínJ.J.Laserna. Experimental determination of laser induced breakdown thresholds of metals under nanosecond Q-switched laser operation. Spectrochimica Acta Part B 53 (1998) 723-730 https://doi.org/10.1016/S0584-8547(98)00107-4

10 L.Torrisi, S. Gammino, L. Andò, V. Nassisi, D. Doria, A. Pedone. Comparison of nanosecond laser ablation at 1064 and 308 nm wavelength. Applied Surface Science (2003) 210(3):262-273. https://doi.org/10.1016/S0169-4332(02)01467-8

11 L. Torrisi, A. Borrielli, D. Margarone. Study on the ablation threshold induced by pulsed lasers at different wavelengths. Nucl. Instrum Meth. B (2007) 255(2):373-379 https://doi.org/10.1016/j.nimb.2006.12.144

12 A. Spiro, M. Lowe, G. Pasmanik. Drilling rate of five metals with picosecond laser pulses at 355, 532, and 1064 nm. Appl. Phys. A (2012) 107: 801. https://doi.org/10.1007/s00339-012-6910-x

13 A.A. Dergachev, A.A. Ionin, V.P. Kandidov, L.V. Seleznev, D.V. Sinitsyn, E.S. Sunchugasheva, S.A. Shlenov. Filamentation of IR and UV femtosecond pulses upon focusing in air. Quantum Electron. (2013) 43 29. https://doi.org/10.1070/QE2013v043n01ABEH015007

14 J. Hoffman, J. Chrzanowska, S. Kucharski, T. Moscicki, I. N. Mihailescu, C. Ristoscu, Z. Szymanski. The effect of laser wavelength on the ablation rate of carbon. Appl. Phys. A (2014) 117, 395. https://doi.org/10.1007/s00339-014-8506-0

15 D. V. Apeksimov, O. A. Bukin, E. E. Bykova, Yu. E. Geints, S. S. Golik, A. A. Zemlyanov, A. A. Il’in, A. M. Kabanov, G. G. Matvienko, V. K. Oshlakov, A. V. Petrov, E. B. Sokolova. Filamentation of the focused Ti: Sapphire laser pulse in air at two harmonics. Plasma Phys. Rep. (2013) 39: 1074. https://doi.org/10.1134/S1063780X13070106

16 T. J. Wang, J. F. Daigle, J. Ju, S. Yuan, R. Li, S. L. Chin. Forward lasing action at multiple wavelengths seeded by white light from a femtosecond laser filament in air. Phys. Rev. A (2013) 88, 053429. https://doi.org/10.1103/PhysRevA.88.053429

17 Yu. E. Geints, A. A. Zemlyanov, A. A. Ionin, D. V. Mokrousova, L. V. Seleznev, D. V. Sinitsyn, E. S. Sunchugasheva. Comparative analysis of post-focal filamentation of focused UV and IR laser pulses in air. Quantum Electron. (2015) 45 321. https://doi.org/10.1070/QE2015v045n04ABEH015640

18 N. L. LaHaye, S. S. Harilal, P. K. Diwakar, A. Hassanein, P. Kulkarni. The effect of ultrafast laser wavelength on ablation properties and implications on sample introduction in inductively coupled plasma mass spectrometry. J. Appl. Phys. (2013) 114, 023103. http://dx.doi.org/10.1063/1.4812491

19 S. M. Wiggins, J. Bonse, J. Solis, C. N. Afonso, K. Sokolowski-Tinten, V. V. Temnov, P. Zhou, D. von der Linde. The influence of wavelength on phase transformations induced by picosecond and femtosecond laser pulses in GeSb thin films. J. Appl. Phys. (2005) 98, 113518. https://doi.org/10.1063/1.2139830

20 X. Zeng, X.L. Mao, R. Greif, R.E. Russo. Experimental investigation of ablation efficiency and plasma expansion during femtosecond and nanosecond laser ablation of silicon. Appl. Phys. A (2005) 80: 237. https://doi.org/10.1007/s00339-004-2963-9

21 A. E. Hussein, P. K. Diwakar, S. S. Harilal, A. Hassanein. The role of laser wavelength on plasma generation and expansion of ablation plumes in air. J. Appl. Phys. (2013) 113, 143305. http://dx.doi.org/10.1063/1.4800925

22 K. Sokolowski-Tinten, J. Bialkowski, A. Cavalleri, M. Boing, H. Schueler, D. von der Linde. Dynamics of femtosecond-laser-induced ablation from solid surfaces. Proc. SPIE 3343, High-Power Laser Ablation, (1998). https://doi.org/10.1117/12.321593

23 T. Y. Choi, C. P. Grigoropoulos. Plasma and ablation dynamics in ultrafast laser processing of crystalline silicon. J. Appl. Phys. (2002) 92, 4918. https://doi.org/10.1063/1.1510565

24 D. Puerto, W. Gawelda, J. Siegel, J. Bonse, G. Bachelier, J. Solis. Transient reflectivity and transmission changes during plasma formation and ablation in fused silica induced by femtosecond laser pulses. Appl. Phys. A (2008) 92. 803. https://doi.org/10.1007/s00339-008-4586-z

25 S. Rapp, J. Rosenberger, M. Domke, G. Heise, H. P. Huber, M. Schmidt. Ultrafast pump-probe microscopy reveals the mechanism of selective fs laser structuring of transparent thin films for maskless micropatterning. Appl. Surf. Sci. (2014) 290, 30 368-372. https://doi.org/10.1016/j.apsusc.2013.11.086

26 M. Garcia-Lechuga, J. Siegel, J. Hernandez-Rueda, J. Solis. Femtosecond laser ablation of dielectric materials in the optical breakdown regime: Expansion of a transparent shell. Appl. Phys. Lett. (2014) 105, 112902. http://dx.doi.org/10.1063/1.4895926

27 I. Carrasco-García, J. M. Vadillo, J. J. Laserna. Visualization of surface transformations during laser ablation of solids by femtosecond pump–probe time-resolved microscopy. Spectrochimica Acta Part B 113 (2015) 30–36. http://dx.doi.org/10.1016/j.sab.2015.08.009

28 I. Carrasco-García, J. M. Vadillo, J. J. Laserna. Monitoring the dynamics of the surface deformation prior to the onset of plasma emission during femtosecond laser ablation of noble metals by time-resolved reflectivity microscopy. Spectrochimica Acta Part B 131 (2017) 1–7. http://dx.doi.org/10.1016/j.sab.2017.02.014

29 B. Rethfeld, K. Sokolowski-Tinten, D. von der Linde, S. I. Anisimov. Timescales in the response of materials to femtosecond laser excitation. Appl. Phys. A (2004) 79: 767. https://doi.org/10.1007/s00339-004-2805-9

30 E.G. Gamaly, A.V. Rode. Physics of ultra-short laser interaction with matter: From phonon excitation to ultimate transformations. Progress in Quantum Electronics 37 (2013) 215–323. http://dx.doi.org/10.1016/j.pquantelec.2013.05.001

31 E. G. Gamaly, A. V. Rode, B. Luther-Davies, V. T. Tikhonchuk. Ablation of solids by femtosecond lasers: Ablation mechanism and ablation thresholds for metals and dielectrics. Physics of Plasmas (2002) 9, 949. http://dx.doi.org/10.1063/1.1447555

32 A. Horn, I. Mingareev, J. Gottmann, A. Werth, U. Brenk. Dynamical detection of optical phase changes during micro-welding of glass with ultra-short laser radiation. Meas. Sci. Technol. 19 (2008) 015302. https://doi.org/10.1088/0957-0233/19/1/015302

33 P. Balling, J. Schou. Femtosecond-laser ablation dynamics of dielectrics: basics and applications for thin films. Rep. Prog. Phys. 76 (2013) 036502. https://doi.org/10.1088/0034-4885/76/3/036502

34 B. Rethfeld, A. Kaiser, M. Vicanek, G. Simon. Femtosecond laser-induced heating of electron gas in aluminium. Appl. Phys. A (1999) 69 [Suppl.], S109–S112. https://doi.org/10.1007/s003399900228

35 N.N. Nedialkov, P.A. Atanasov, S. Amoruso, R. Bruzzese, X. Wang. Laser ablation of metals by femtosecond pulses: Theoretical and experimental study. Appl. Surf. Sci. 253 (2007) 7761–7766. https://doi.org/10.1016/j.apsusc.2007.02.083

36 E. G. Gamaly. The physics of ultra-short laser interaction with solids at non-relativistic intensities. Physics Reports 508 (2011) 91–243. https://doi.org/10.1016/j.physrep.2011.07.002

37 K. Sokolowski-Tinten, J. Bialkowski, A. Cavalleri, D. von der Linde. Observation of a transient insulating phase of metals and semiconductors during short-pulse laser ablation. Applied Surface Science 127–129 (1998). 755–760. https://doi.org/10.1016/S0169-4332(97)00736-8

38 S. K. Sundaram, E. Mazur. Inducing and probing non-thermal transitions in semiconductors using femtosecond laser pulses. Nature Materials (2002) 1, pages 217–224.

39 N. M. Bulgakova, I. M. Burakovi, Y. P. Meshcheryakov, R. Stoian, A. Rosenfeld, I. V. Hertel. Theoretical Models and Qualitative Interpretations of Fs Laser Material Processing. JLMN-Journal of Laser Micro/Nanoengineering (2007) 2, 1, 76-86.

40 M. V. Shugaev, C. Wu, O. Armbruster, A. Naghilou, N. Brouwer, D. S. Ivanov, T. J. Y. Derrien, N. M. Bulgakova, W. Kautek, B. Rethfeld, L. V. Zhigilei. Fundamentals of ultrafast laser–material interaction. Ultrafast Laser Synthesis and Processing of Materials (2016) 41, 12, 960-968. https://doi.org/10.1557/mrs.2016.274

41 D. von der Linde, K. Sokolowski-Tinten. The physical mechanisms of short-pulse laser ablation. Applied Surface Sci. 154–155 (2000). 1–10. https://doi.org/10.1016/S0169-4332(99)00440-7

42 N. E. Bykovskii, Y. V. Senatskii. On the Formation Mechanism of Interference Rings in the Ablation Area on the Condensed Medium Surface under Irradiation with Femtosecond Laser Pulses. Phys. Solid State (2018) 60: 404. https://doi.org/10.1134/S1063783418020087

43. Marina López-Claros, José M. Vadillo and J. Javier Laserna. Determination of plasma ignition threshold fluence during femtosecond single-shot laser ablation on metallic samples detected by optical emission spectroscopy. J. Anal. At. Spectrom., 2015, 30, 1730–1735. https://doi.org/10.1039/c5ja00076a

FIGURES

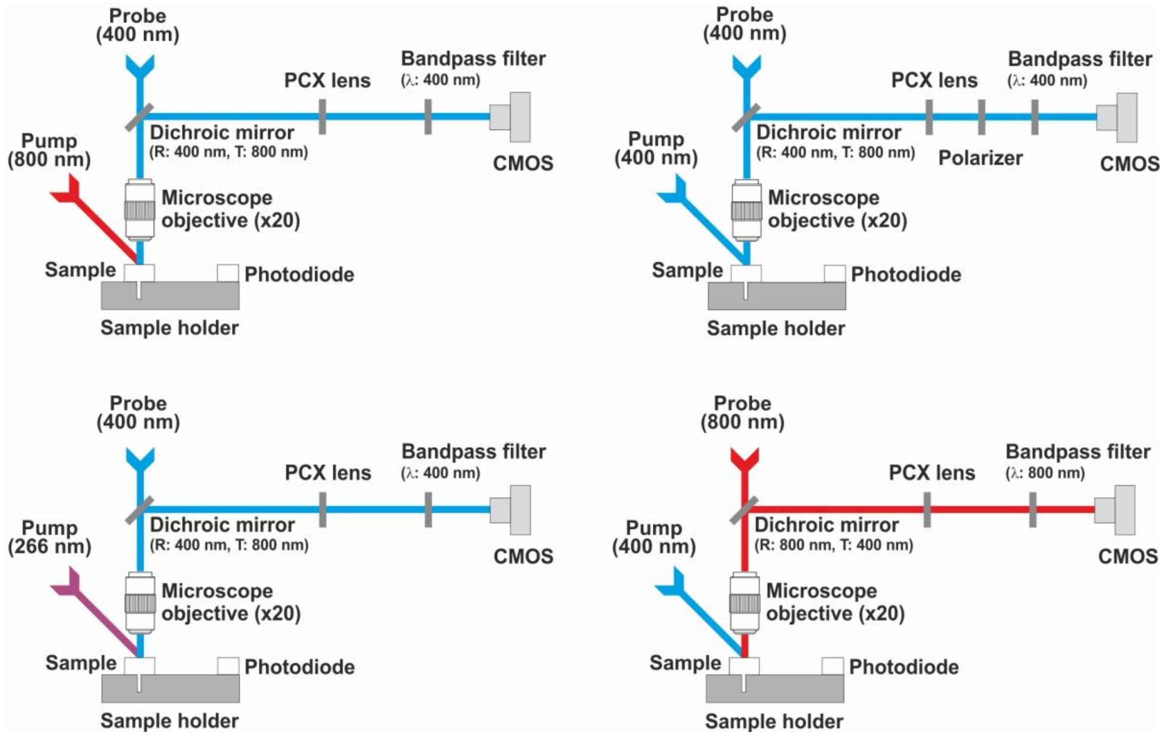

Figure 1. Details of the specific configurations for the different wavelength combinations of the pump and probe beams used for the measurements.

Figure 2

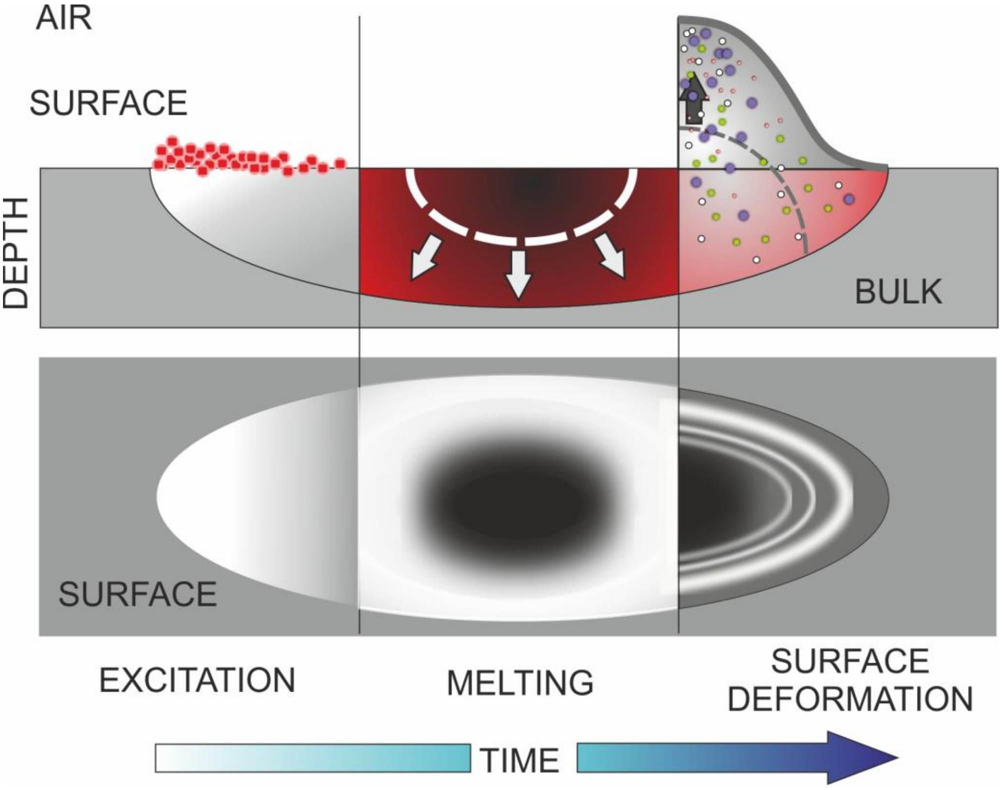

Figure 2. Schematic side and front views of the general processes occurring after femtosecond laser irradiation. Left: excitation and generation of electron–hole plasma; Center: melting of the irradiated area; Right: expansion of the molten surface by the encapsulated vaporized material.

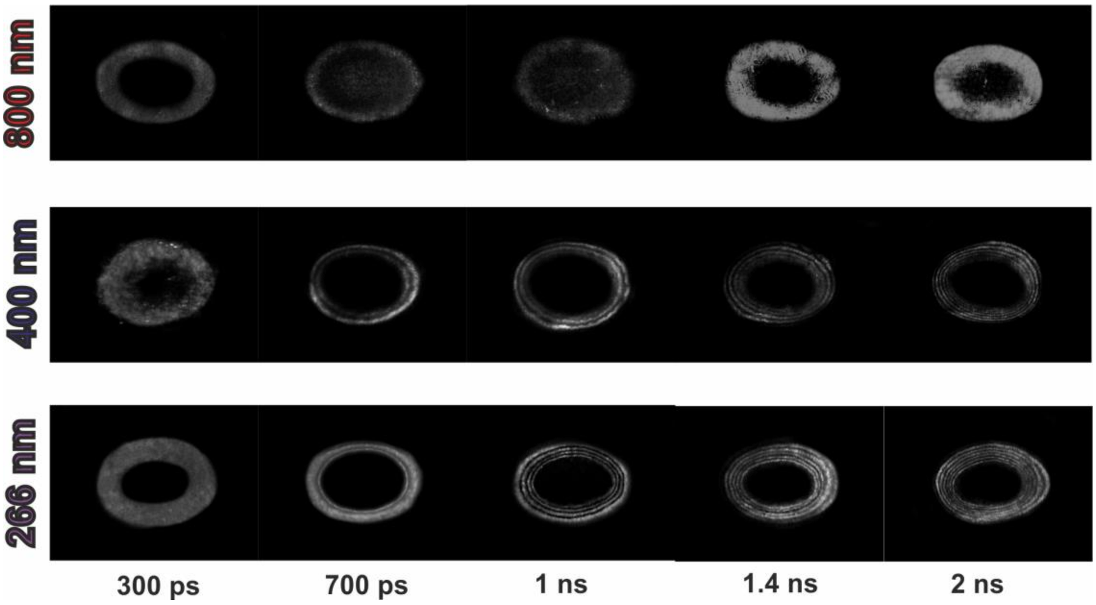

Figure 3. Temporal evolution of the irradiated surface using different excitation wavelengths. Pump energy 20 μJ. Probe wavelength 400 nm.

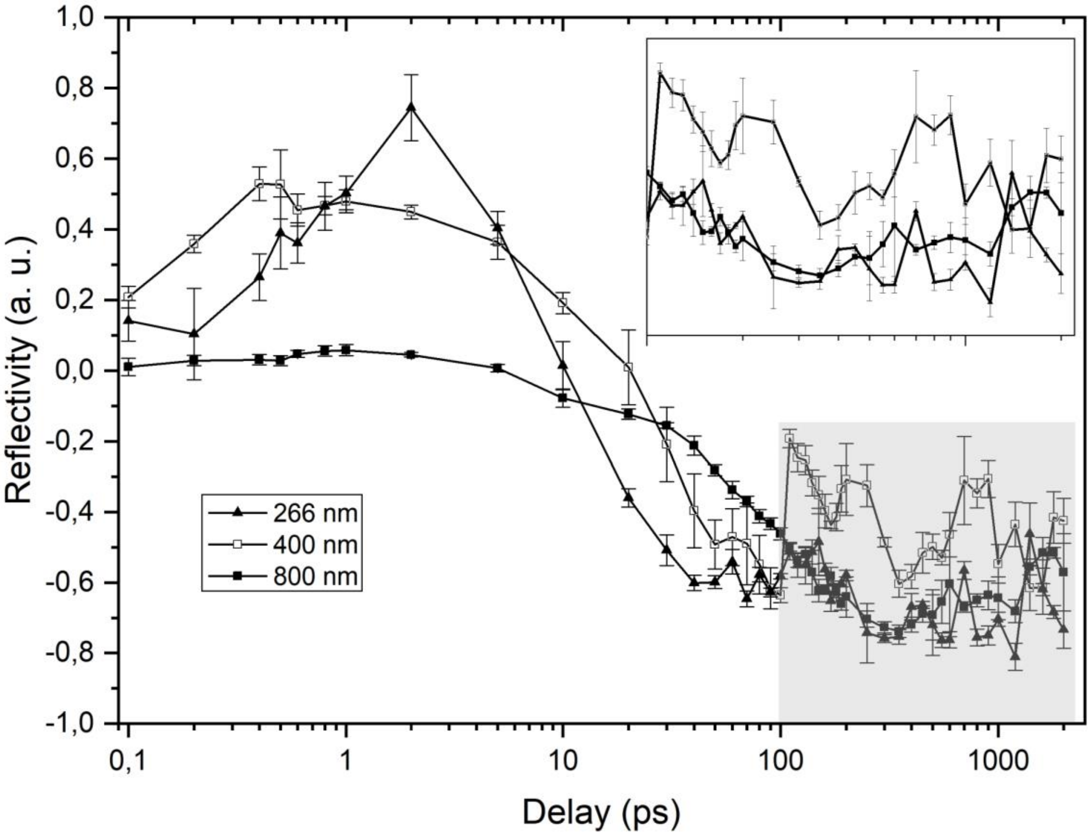

Figure 4. Normalized surface reflectivity with 400 nm probe illumination, after 20 μJ/pulse excitation at (a) 266 nm, (b) 400 nm, and (c) 800 nm.

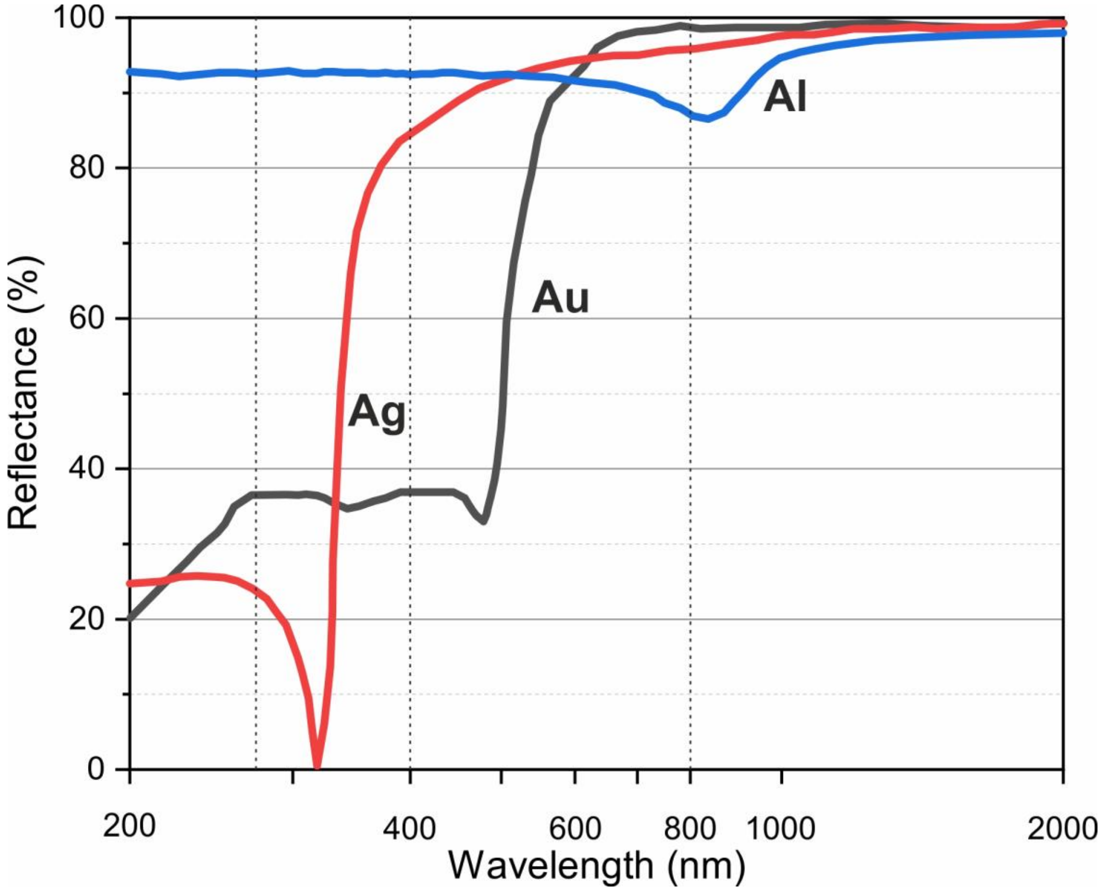

Figure 5. Variation of the reflectance with the incident wavelength for Au, Ag and Al.

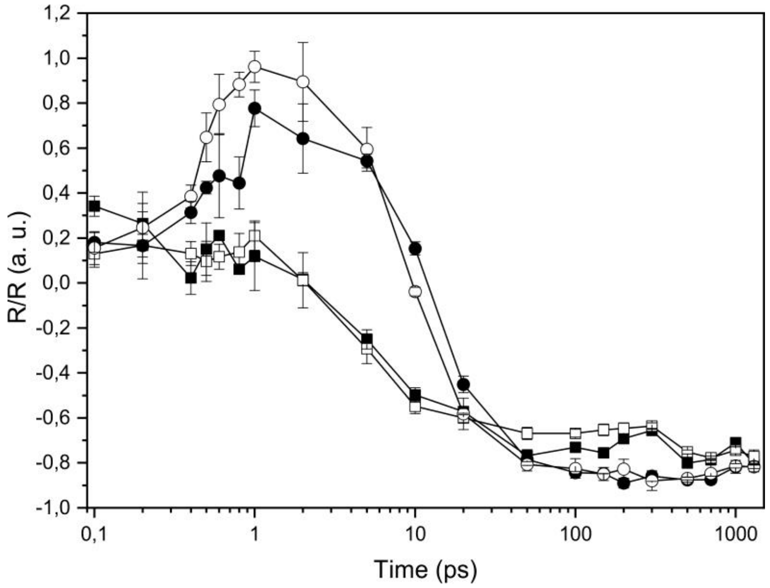

Figure 6. Temporal evolution of gold target normalized surface reflectivity using different pump/probe configurations. Squares: 400/800 nm; Circles: 800/400 nm. Solid dots: 50 μJ/pulse. Open dots: 100 μJ/pulse.

FIGURE CAPTIONS

Figure 1: Details of the specific configurations for the different wavelength combinations of the pump and probe beams used for the measurements.

Figure 2: Schematic side and front views of the general processes occurring after femtosecond laser irradiation. Left: excitation and generation of electron–hole plasma; Center: melting of the irradiated area; Right: expansion of the molten surface by the encapsulated vaporized material.

Figure 3: Temporal evolution of the irradiated surface using different excitation wavelengths. Pump energy 20 μJ. Probe wavelength 400 nm.

Figure 4: Normalized surface reflectivity with 400 nm probe illumination, after 20 μJ/pulse excitation at (a) 266 nm, (b) 400 nm, and (c) 800 nm.

Figure 5: Variation of the reflectance with the incident wavelength for Au, Ag and Al.

Figure 6: Temporal evolution of gold target normalized surface reflectivity using different pump/probe configurations. Squares: 400/800 nm; Circles: 800/400 nm. Solid dots: 50 μJ/pulse. Open dots: 100 μJ/pulse.